Dual Plasmonic Nanostructures for High Performance Inverted Organic Solar Cells

Xuanhua Li, Wallace C. H. Choy, Lijun Huo, Fengxian Xie, Wei E. I. Sha, Baofu Ding, Xia Guo, Yongfang Li, Jianhui Hou,* Jingbi You, and Yang Yang*

Polymer-fullerene-based bulk heterojunction (BHJ) solar cells have many advantages, including low-cost, low-temperature fabrication, semi-transparency, and mechanical flexibility.[1,2] However, there is a mismatch between optical absorption length and charge transport scale.[3,4] These factors lead to recombination losses, higher series resistances, and lower fill factors. Attempts to optimize both the optical and electrical properties of the photoactive layer in organic solar cells (OSCs) inevitably result in a demand to develop a device architecture that can enable efficient optical absorption in films thinner than the optical absorption length.[5,6] Here, we report the use of two metallic nanostructures to achieve broad light absorption enhancement, increased short-circuit current (J_{sc}), and improved fill factor (*FF*) simultaneously based on the new small-bandgap polymer donor poly{[4,8-bis-(2-ethyl-hexyl-thiophene-5-yl)-benzo[1,2-b:4,5-b′]dithiophene-2,6-diyl]-*alt*-[2-(2′-ethyl-hexanoyl)-thieno[3,4-b]thiophen-4,6-diyl]} (PBDTTT-C-T) in BHJ cells.[7] The dual metallic nanostructure consists of a metallic nanograting electrode as the back reflector and metallic nanoparticles (NPs) embedded in the active layer. Consequently, we achieve the high power conversion efficiency (PCE) of 8.79% for a single-junction BHJ OSC.

Recently, plasmonic nanostructures have been introduced into solar cells for highly efficient light harvesting.[5,8–17] Two types of plasmonic resonances, surface plasmonic resonances (SPRs)[18–22] and localized plasmonic resonances (LPRs),[11–14] can be used for enhancing light absorption. Metallic grating-based light-trapping schemes have been investigated in traditional inorganic photovoltaic cells.[18–20] For metallic nanogratings, which can support SPRs, it is still challenging to experimentally demonstrate the enhancement of PCE in OSCs owing to the obvious issue of solution processing of nanometer-scale-thick and conformal OSC layers on topographical surfaces.[6]

Although a few light-trapping schemes based on periodic patterning have been reported, such as microprism substrates and buried nanoelectrodes,[15,17,23,24] and enhancement in optical absorption has been demonstrated in OSCs, there are some concerns about processing bottlenecks and drawbacks in making periodic patterns in polymers. First, traditional embossing in polymers using nanoimprinting methods (such as pattern replication by the nonwetting-template method) is a process at an elevated temperature.[17,23,24] Such an annealing step is not universally desirable for all BHJ materials and may cause unexpected damage to the films. Second, the embossing step poses bubble/void concerns, which will lead to an unexpectedly irregular film. Lastly, and importantly, many recent high-performance materials do not need, or even degrade during, thermal annealing,[2,7,25,26] so the traditional thermal nanoimprinting method cannot be used to produce the grating nanostructures in OSCs made from such polymers with improved PCE. Here, a room-temperature vacuum-assisted nanoimprinting method is proposed to effectively solve these issues. For the electrical properties, although nanostructured back reflectors can improve the light absorption of solar cells, there is room to improve the electrical properties. For instance, *FF* of reported OSCs with integrated back grating electrode of nanometer-scale pitch is typically reduced compared to the corresponding flat control devices.[15,23] In this work, by adopting inverted device structures and the room-temperature vacuum-assisted nanoimprinting method, we demonstrated OSCs with improved optical absorption, J_{sc}, *FF*, and PCE.

Besides the improvement by the metallic grating, there have been reports of optical absorption enhancement by incorporating metallic NPs into the hole transport layer,[8,27] active layer,[9,11,13,28] or all polymer layers[12] of single-junction OSCs, and the interconnecting layer of tandem OSCs,[14] resulting in improved PCE. Metallic NPs can induce LPRs. LPRs and SPRs typically have narrow but different resonance wavelength regions.[29] Since sunlight is a broadband light source, it is desirable to extend the wavelength region of the enhanced light absorption by using plasmonic nanostructures. In addition, there is no report on introducing both LPRs and SPRs in one device structure for broadband light absorption enhancement.

Here, we propose and demonstrate experimentally dual metallic nanostructures that are composed of Au NPs (i.e., for LPR) embedded in the active layer and a Ag nanograting electrode (i.e., for SPR) as the back reflector in inverted OSCs. Through the collective excitation of Floquet modes, SPR, LPR, and their hybridizations, we enable broadband absorption enhancement. Moreover, our design aims at achieving positive electrical effects

X. H. Li, Prof. W. C. H. Choy, F. X. Xie,
Dr. W. E. I. Sha, Dr. B. F. Ding
Department of Electrical and Electronic Engineering
The University of Hong Kong
Pokfulam Road, Hong Kong, China
E-mail: chchoy@eee.hku.hk (Choy)
Prof. L. J. Huo, X. Guo, Prof. Y. F. Li, Prof. J. H. Hou
Institute of Chemistry
Chinese Academy of Sciences
Beijing 100190, China
E-mail: hjhzlz@iccas.ac.cn (Hou)
Dr. J. B. You, Prof. Y. Yang
Department of Materials Science and Engineering
University of California
420 Westwood Plaza, Los Angeles, CA 90095, USA

DOI: 10.1002/adma.201200120

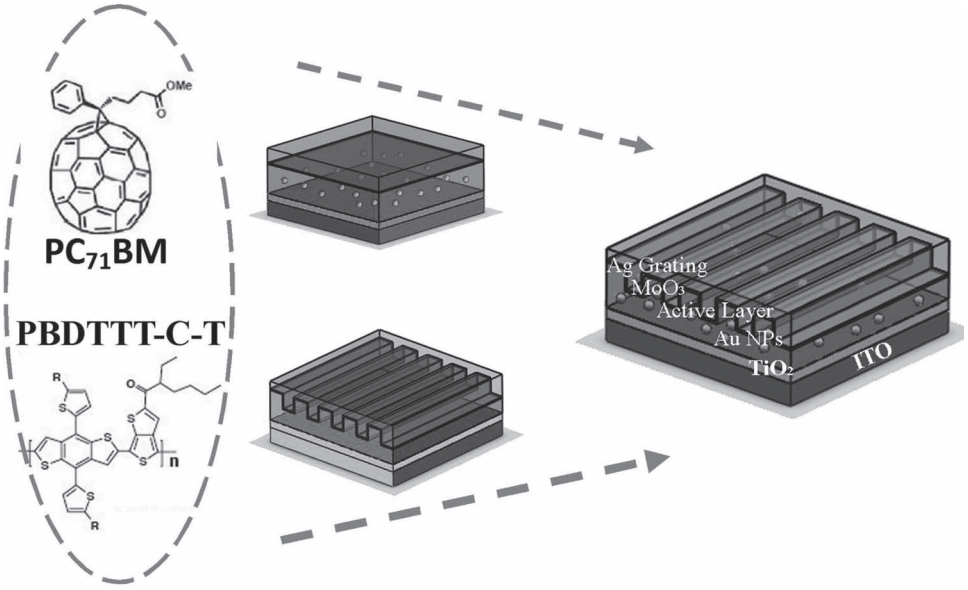

Figure 1. Chemical structures of PBDTTT-C-T and $PC_{71}BM$ (left). Schematic of the device structure: NP device (top), grating device (bottom), and dual metallic structural device (right).

simultaneously. Showing positive electrical effects is important because the enhancement of light trapping and optical absorption should not be the sole target in a practical optical design. It is urged to consider an equally critical question in designing device structures: what is the approachable optical device structure for realizing both enhanced optical absorption and positive electrical effects. In our dual plasmonic OSCs, we 1) clarify the fundamental physics of various intriguing optical phenomena, 2) discuss the roles of the metallic nanostructures in improving the optical and electrical properties of OSCs, and 3) demonstrate the accumulated electrical and optical improvements that can realize considerable absorption enhancement and achieve an 8.79% PCE in inverted OSCs.

Dual metallic nanostructure (Au NPs plus Ag nanograting) OSCs with a device structure of ITO/TiO_2 (20 nm)/PBDTTT-C-T:$PC_{71}BM$ + Au NPs (100 nm) MoO_3 (10 nm)/Ag nanograting electrode were fabricated as described in **Figure 1**. We studied the optical and electrical effects by using various concentrations of Au NPs with diameters of 20 nm (NPs20) and 50 nm (NPs50) and Ag nanogratings with mask grating periodicities of 750 nm (G750) and 350 nm (G350). Transmission electron microscopy (TEM) and scanning electron microscopy (SEM) images of the Au NPs and Ag nanograting are shown in Figures S1 and S2, respectively, in the Supporting Information. Because the OSC performance of the new material PBDTTT-C-T will drop after thermal annealing, the traditional polydimethylsiloxane (PDMS) nanoimprinting methods, which need thermal annealing, cannot be used to produce grating features on these materials. In this work, we propose the use of a room-temperature vacuum-assisted nanoimprinting method to directly produce the pattern on the active layer with a G750 grating (see the Experimental Section and Figure S3 in the Supporting Information). The vacuum process can remove the unwanted bubbles/voids introduced at the interface between the organic layer (of the device) and the PDMS pattern and extract the solvent of the polymer blend to form a solid-state polymer film without annealing. The polymer blend film without and with the vacuum process are shown in **Figure 2**a,b, respectively. We can see that the film made under vacuum is much smoother. Importantly, our proposed approach does not involve any annealing of organics, which is favorable for all organic materials but particularly for those which will degrade under annealing.

The morphology of the dual plasmonic OSC structures was investigated. An atomic force microscopy (AFM) image of the active layer and SEM cross-section image of OSCs with NPs50 and G750 (NPs50+G750) are shown in Figure 2c,d, respectively. An AFM image of the smooth active layer of the control OSCs is shown in Figure S4 in the Supporting Information for reference. When the anode (MoO_3 and Ag) is evaporated on the nanostructured active layer subsequently, the anode/active layer interface will closely follow the surface profile of the active layer, hence the grating features will be present on the Ag anode. The Au NPs and the nanograting structure electrode are clearly observed in the cross-sectional SEM image. Interestingly, the Au NPs are located at the bottom of the active layer, which reduces the possibility of a short circuit due to direct contacts of Au NPs and the Ag nanograting.

The current density–voltage (J–V) characteristics of different structural devices are shown in **Figure 3**, and the photovoltaic parameters are listed in **Table 1**. In order to understand the mechanisms of PCE improvement of the dual metallic nanostructural OSCs, we first optimized OSC performance with one type of metallic nanostructure (i.e., Au NPs only or Ag nanograting only). Then we investigated the effects of the dual metallic nanostructures (i.e., both Au NPs and Ag nanograting in one single OSC) on the PCE improvement. For Ag-nanograting-only OSCs, we can see that PCE obviously improves from 7.59% (control, flat OSCs) to 8.38% (G750 OSCs). PCE improvements originate from the improvements of J_{sc} and FF. The higher FF is a consequence of the nanoimprinted pattern increasing

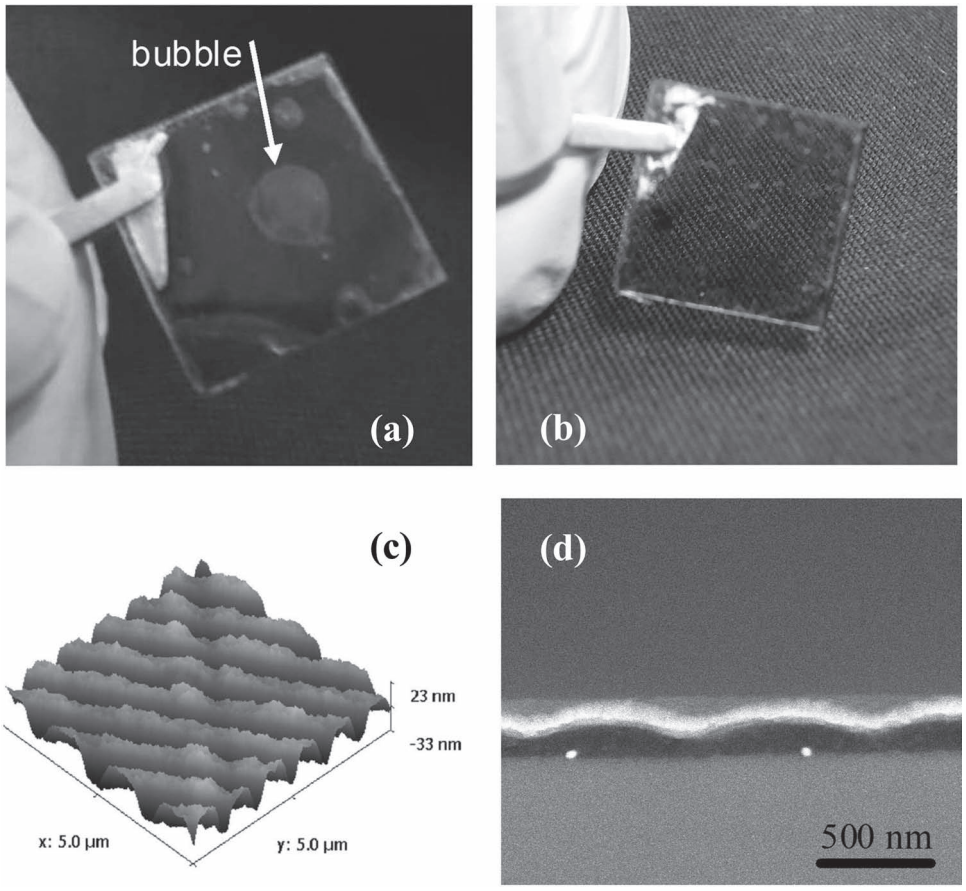

Figure 2. Patterned PBDTTT-C-T: $PC_{71}BM$ polymer blend formed a) without and b) with vacuum process. Bubbles are formed on the film without the vacuum process. c) AFM image of PBDTTT-C-T: $PC_{71}BM$ active layer with 1 wt% embedded Au NPs (50 nm) at the active layer and patterned with a nanograting (grating period = 750 nm). d) Cross-sectional SEM image of NPs50+G750 device, with incorporated 50 nm Au NPs and back silver grating with 750 nm period.

the interface area.[8,30,31] Besides, the series resistance (R_s) of the devices decreases from 19.43 Ω cm2 (control, flat OSCs) to 12.18 Ω cm2 (G750 OSCs), which also contributes to the higher FF.[8,9,11,12] From the transient photogenerated voltage (TPV)[32]

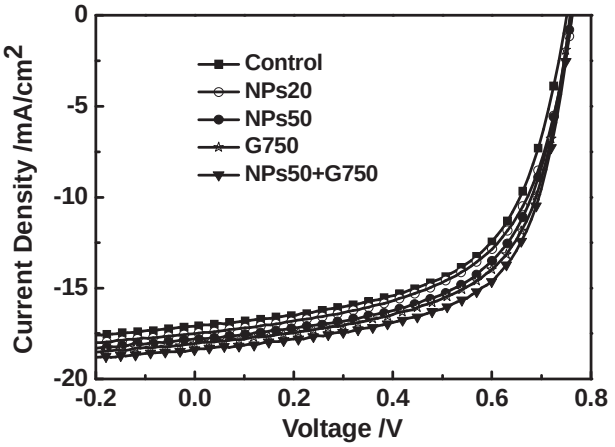

Figure 3. *J–V* characteristics of devices with different structures measured under AM 1.5 illumination at 100 mW cm^{-2}.

of the OSCs with a Ag nanograting, we find that the spectrum overlaps with that of the control device, as shown in Figure S5 (Supporting Information). This means that there is no degradation in the ratio of hole and electron mobilities.

To elucidate the light-trapping nature of our grating device, we extracted the absorption from diffuse reflection (R) and transmission (T), using $1 - R - T$, and incident photon-to-electron conversion efficiency (IPCE) of OSCs as shown in **Figure 4**a,b. As compared to control OSCs, the extracted absorption of the nanograting OSC is significantly improved, which indicates that more light is absorbed for nanograting OSCs, which contributes to the improvement of IPCE as shown in Figure 4b. To further clarify our data, we calculated the enhancement factor of the extracted absorption and IPCE of devices with and without a grating, as shown in Figure 4a,b. The trend of the IPCE enhancement factor generally shows the features of the absorption enhancement factor, although the enhanced carrier collection with increased interfacial area of the nanograting OSCs also contributes to the improvement of IPCE. We can also observe several absorption enhancement regions, including the wavelength regions around 380, 600, and 800 nm. To understand the absorption enhancement, we constructed a theoretical model of the OSCs by rigorously solving

Table 1. Photovoltaic parameters of the OSCs with different metallic nanostructures under AM 1.5G illumination at 100 mW cm^{-2}. R_S is derived from the slope of the *J–V* curves in the dark at 1 V.

Device Description	V_{OC} [V]	J_{SC} [mA cm^{-2}]	*FF* [%]	PCE [%]	R_S [Ω cm^2]
Flat (control)	0.76 ± 0.01	17.09 ± 0.09	58.43 ± 0.43	7.59 ± 0.08	19.43 ± 0.68
Optimized grating G750 only	0.76 ± 0.01	18.04 ± 0.35	61.17 ± 1.02	8.38 ± 0.20	12.18 ± 1.6
Optimized Au NPs (NPs20) only	0.77 ± 0.01	17.51 ± 0.35	58.10 ± 1.02	7.83 ± 0.20	17.24 ± 0.65
Optimized Au NPs (NPs50) only	0.76 ± 0.01	17.78 ± 0.35	60.34 ± 1.02	8.11 ± 0.20	15.56 ± 0.94
Optimized Au NPs (NPs50) + grating (G750)	0.76 ± 0.01	18.39 ± 0.20	62.87 ± 0.66	8.79 ± 0.15	4.32 ± 0.86

Maxwell's equations as described in the Experimental Section. From the simulation results, we understand that the enhancement in the region around 380 nm can be attributed to the Wood's anomaly observed from the peak of power flux in the grating layer.[10] The regions around 600 nm and 800 nm are attributed to SPR hybridized with different Floquet modes of the Ag nanograting. The near-field profile Wood's anomaly is shown in **Figure 5**a and the near profiles of the hybridized SPRs are shown in Figure 5b,c. It should be noted that the Rayleigh anomaly peak of 750 nm for the mask grating (G750) is red-shifted to around 800 nm experimentally (as shown in Figure 4a) because of geometric deviations of the patterned active layer from the mask grating that occur during the nanoprinting process. Further details can be found in Figures S6–S8 and the corresponding discussion in the Supporting Information.

Besides using the mask grating with a periodicity of 750 nm, we also made patterned OSCs using a mask grating with a periodicity of 350 nm; the results are shown in Table S1 and Figure S9 in the Supporting Information. We find that the imprinted pattern of the 350 nm grating on the active layer of OSCs (see Figure S10 in the Supporting Information) is not as good as that of the 750 nm grating (see Figure S7) and the performance

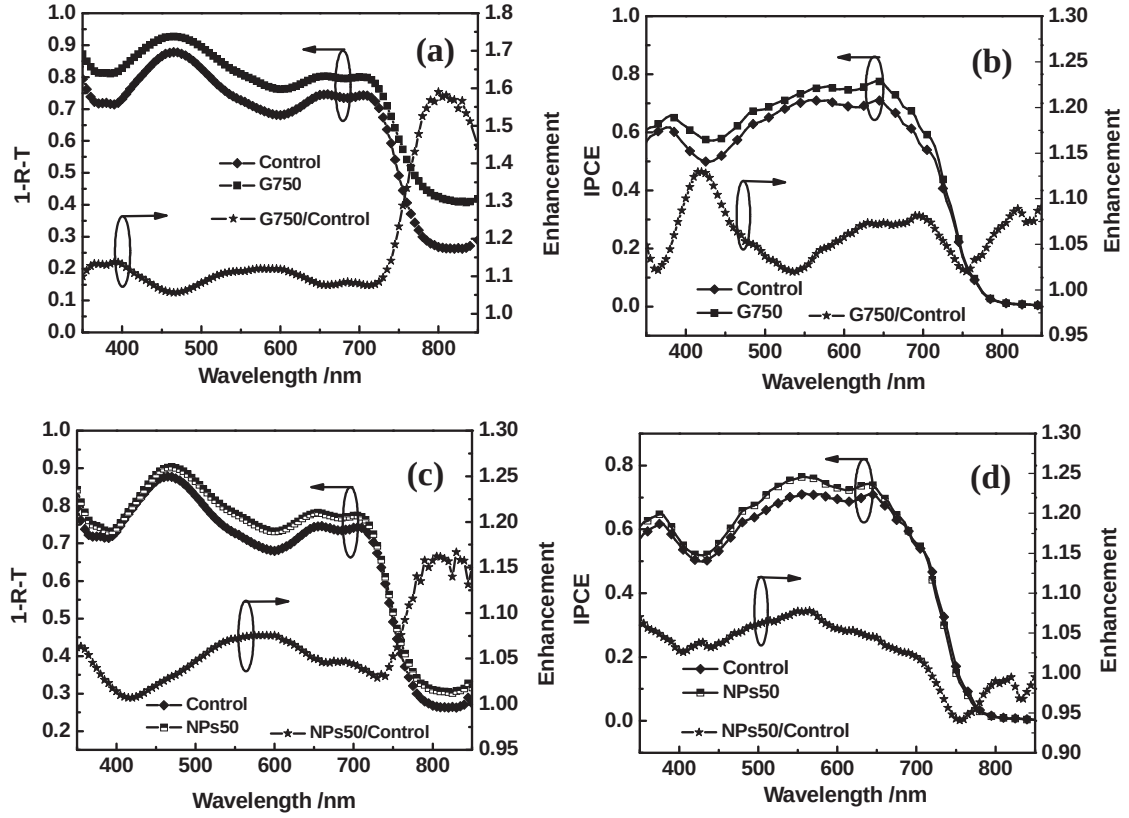

Figure 4. a) The extracted absorption of OSCs (1 – diffuse reflection (*R*) – diffuse transmission (*T*)) with and without G750 nanograting structure and the absorption enhancement, i.e., (1 – *R* – *T* of G750 OSC)/(1 – *R* – *T* of control flat OSC). b) IPCE of the two OSCs and the enhancement, i.e., (IPCE of G750 OSC)/(IPCE of control flat OSC). c) Reflected absorption of OSCs with and without 50 nm Au NPs and the enhancement. d) IPCE of the two OSCs and the enhancement.

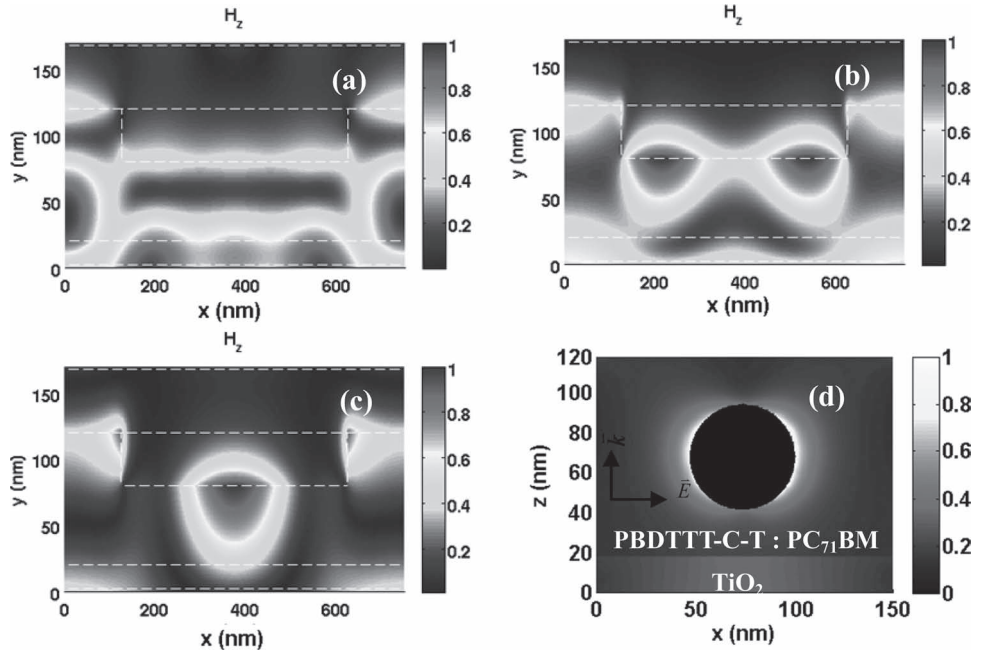

Figure 5. a) Near-field profile of Wood's anomaly at 380 nm. b,c) Near-field profiles of SPR hybridized with Floquet modes at 610 nm (b) and 810 nm (c). d) Near-field profile of 50 nm Au NPs (NPs50) in OSCs.

enhancement of OSC patterned by the 350nm grating (see Table S1) is not as high as that of the 750 nm grating. In addition, the physical mechanism governing the optical improvement of the OSCs patterned by the 350 nm grating is similar to that of the 750 nm grating. Therefore, we focus on the 750 nm grating in dual plasmonic structures.

Regarding the study of Au NPs embedded in the active layer of OSCs, since the active layer thickness of the optimized flat (control) device is about 100 nm and the nanograting will be patterned on the active layer, too large Au NPs may easily cause short circuiting of the devices. In this work, we selected two sets of NPs with size 20 nm and 50 nm to optimize the NP device. The OSCs have improved PCE with values of 7.83% and 8.11% (PCE of control OSC = 7.59%) when the optimized concentration of 2 wt% of 20nm or 50nm Au NPs is incorporated in the active layer as shown in Table 1. Details of device performances, including *J–V* characteristics, light absorption, IPCE, and device parameters for OSCs with various concentrations of 20 nm Au NPs embedded in the active layer are shown in Figures S11, S13a,c,e, and Table S2, while the detailed performance of 50 nm Au NPs are shown in Figures S12, S13b,d f, and Table S3 in the Supporting Information. The distributions of Au NPs in the active layer with different concentrations of Au NPs are also shown in Figures S14 and S15 (Supporting Information). Consequently, Au NPs with a diameter of 50 nm offer better PCE owing to the larger improvement of J_{sc} (17.78 mA cm^{-2}) and *FF* (0.603), as shown in Table 1. The higher J_{sc} and *FF* are due to the improved charge transport and decreased R_s (15.56 Ω cm^2).[8,9,11,12] The improved charge transport can be shown from the improved hole mobility from 7.4×10^{-4} cm^2 V^{-1} s^{-1} (control) to 1.76×10^{-3} cm^2 V^{-1} s^{-1} determined by the space-charge-limited current (SCLC) model[33] together with hole-dominated devices with structures of ITO/ PEDOT:PSS/ PBDTTT-C-T:$PC_{70}BM$ (100 nm) with and without 2 wt% Au NPs (50 nm)/ Au. Similarly, the electron mobility increases from 2.69×10^{-3} cm^2 V^{-1} s^{-1} (control) to 3.49×10^{-3} cm^2 V^{-1} s^{-1} determined from electron-dominated devices with structures of ITO/ TiO_2/ PBDTTT-C-T:$PC_{71}BM$ with and without 2 wt% Au NPs (50 nm)/ Ca/ Al (see Figure S16 in Supporting Information). Moreover, from TPV results as shown in Figure S5 in the SI, it is interesting to note that the TPV spectrum of the NPs50 OSC significantly changes from that of the control OSC. By studying the ratio of the slow decay slope and the fast decay slope (i.e., τ_{slow}/τ_{fast}), we can observe that the value of τ_{slow}/τ_{fast} considerably reduces to 3.9 from 12 (control). This indicates that the electron and hole mobilities are more balanced in the NPs50 OSC than in the control device, which contributes to the improvement of J_{sc} and *FF*.

In order to understand the optical effects of Au NPs on the improvement of J_{sc}, we conducted a theoretical study on the device structure with Au NPs embedded in the active layer of OSCs. We found that LPR is excited, which can contribute to absorption enhancement as shown in Figures 4c and d. The strong near field caused by LPRs from Au NPs penetrated into the active layer, as shown in Figure 5d. Together with the scattering effects of Au NPs coupled to waveguide modes, the absorption and IPCE improve, as shown in Figures 4c and d, and thus contribute to the improvement of J_{sc}.

After studying the individual effects of Au NPs and a Ag nanograting on OSCs, we studied the effects of the dual plasmonic structure. Since the optimized NPs50 OSC offers greater performance improvement than the optimized NPs20 OSC, we investigated the dual plasmonic nanostructures of NPs50+G750 with different concentrations of NPs50. Details of the results can

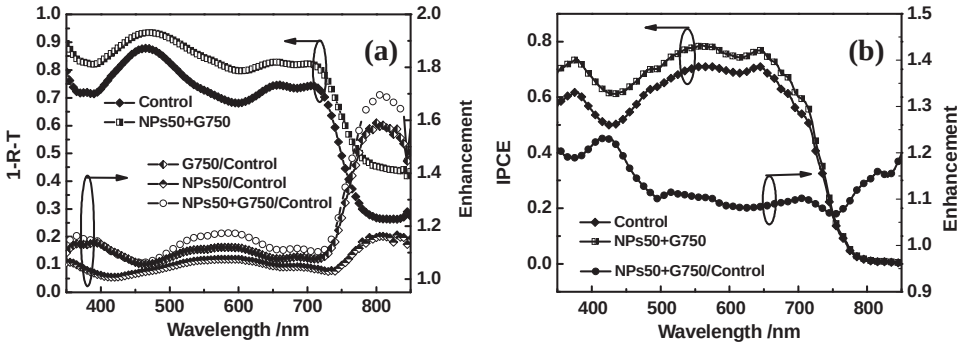

Figure 6. a) The extracted absorption (i.e., $1 - R - T$) of the control flat OSC and NPs50+G750 OSC, and the absorption enhancement of NPs50+G750, G750, and NPs50 compared to the control flat OSC. b) IPCE of the control flat OSC and NPs50+G750 OSC and the IPCE enhancement of NPs50+G750 OSC compared to the control flat OSC.

be found in Table S4 and Figure S17 in the Supporting Information. Our results show that PCE reaches the maximized value of 8.79% as *FF* and J_{sc} increase from 0.584 and 17.09 mA cm^{-2} (control OSC) to 0.629 and 18.39 mA cm^{-2}, respectively, as listed in Table 1. The enhancements can be explained by the electrical improvements offered by the Ag nanograting and Au NPs as described previously, including the larger interface area from the nanograting pattern, the better electron and hole balance from the Au NPs, and the lower series resistance from both the nanograting and Au NPs. Regarding the optical effects from the dual plasmonic structures, a similar increasing trend is observed from the absorption enhancement and IPCE enhancement of OSCs with and without dual metallic nanostructure in **Figures 6**a and b. By plotting together the absorption enhancement spectra of Au NPs only, Ag nanograting only, and combined Au NPs and Ag nanograting, as shown in Figure 6a, we can confirm that the absorption enhancement of metallic NPs and nanogratings combine, contributing to the improvement of J_{sc} and PCE in the OSC with dual plasmonic nanostructure. To the best of our knowledge, this is the first time that metallic NPs and nanogratings have been combined to improve absorption, J_{sc}, *FF*, and PCE of OSCs.

Concerning the use of dual plasmonic structures of metallic NPs and a nanograting for broadening the wavelength region of absorption enhancement, we find that Au NPs offer strong absorption enhancement in the region of 480–600 nm, whereas the Ag grating has a greater impact on absorption at wavelength regions below 400 nm and above 600 nm. Therefore, we successfully introduced these two metallic nanostructures to complement each other in a single OSC unit to enhance the absorption over a larger wavelength region (i.e., achieving a broadband absorption enhancement).

To further demonstrate that plasmonic effects play an important role in the performance of OSCs, we calculated the integrated optical absorption from 300 nm to 900 nm for OSCs (which is commonly called the generation rate) in the AM 1.5 sun spectrum. From Figure S18, we can clearly see that the generation rate is significantly improved in the region near to the grating electrode as a result of the plasmonic resonances. Besides, in the region $0 \le y \le 30$ nm,where y is the thickness of active layer ($y = 0$ refers to the interface between active layer and TiO_2) of the device as shown in Figure S18, the generation rate is also improved considerably owing to the constructive interference between SPRs and incident waves, which can be explained by the reciprocal theorem in electrodynamics. For LPRs, Figure S19 shows the generation rate of the OSC with Au NPs embedded in the active layer. The generation rate is significantly enhanced in the neighboring region of the Au NP along the polarization direction of the electric field. Hence, the generation rate and the short-circuit current will be significantly increased by metallic gratings and NPs.

In conclusion, dual metallic nanostructures are demonstrated in single OSC units by simultaneously incorporating Au NPs into the active layer and fabricating the Ag nanograting electrode by means of the newly proposed room-temperature vacuum-assisted nanoimprinting method. Apart from the waveguide modes and diffraction, we simultaneously introduce hybridized SPR (from the Ag nanograting) and LPR (from the Au NPs) to successfully achieve a broadband absorption enhancement. The detailed mechanism has been described with our theoretically studies. As a consequence, we improved PCE to the very high value of 8.79% by improving both optical properties and electrical properties of OSCs by introducing dual plasmonic nanostructures, which will contribute to the practical application of OSCs for photovoltaics.

Experimental Section

Device Fabrication: The concentration of the polymer/$PC_{70}BM$ (1:1.5, weight ratio) blend solution used to form the active layer by spin-coating was 10 mg mL^{-1}. *o*-Dichlorobenzene was used as the solvent and 3% (v/v) DIO (1, 8-diiodooctane) was used as an additive to improve photovoltaic performance.[7]

Devices were fabricated with the structure ITO/TiO_2 (20 nm)/ active layer with or without Au NPs/ MoO_3 (10 nm)/Ag (with or without grating) (80 nm). ITO glasses were cleaned using a standard procedure. A thin layer (20 nm) of TiO_2 was deposited on the ITO by spin-coating. These samples were then dried at 150 °C for 30 min. Subsequently, polymer solution was spin-coated at 900 rpm for 60 s on top of the TiO_2 layer. The optimized active layer thickness is about 100 nm. The synthesis of Au NPs with 20 nm and 50 nm size followed the sodium citrate reduction method.[8,12,34] The different weight ratios (wt%) of the Au NPs were determined only by considering the weight of PBDTTT-C-T. In order to ensure the easy release of the replica with high reproducibility in the nanoimprinting process, we used flexible PDMS as an elastomeric mold for conformal contact with the substrate. To inscribe the pattern

on the active layer, the PDMS mold was put in conformal contact with the active layer. Since the PBDTTT-C-T film would degrade after annealing, we proposed the room-temperature vacuum-assisted PDMS nanoimprinted method (Figure S3 in the Supporting Information). After the PDMS mold had been placed on the active layer, the whole sample was put into a vacuum chamber at 10^{-2} Torr for 30 min. After removal of the PDMS mold, MoO_3 (10 nm) and silver (100 nm) layers were thermally evaporated onto the active layer with a pattern at a pressure of 10^{-6} Torr.

Characterization of Solar Cells and Thin Films: The thickness of the polymer sample was measured using a Dektak alpha-step profiler. The morphology of the sample was characterized using AFM (Asylum Research MFP-3D) in tapping mode, SEM (Hitachi S-4800), and TEM (Philips Tecnai G220 S-TWIN). The diffuse reflection and transmission spectra were measured using a goniometer combined with a CCD spectrometer and integrating sphere. The TPVs were measured using a picosecond pulse laser and digital storage oscilloscope from Agilent Technologies (DSO71048). *J–V* characteristics and IPCE were measured by methods described elsewhere.[8,12]

Theoretical Modeling: To find a rigorous solution to Maxwell's equations, the finite-difference frequency-domain (FDFD) method with the Yee lattice was adopted to model the dual plasmonic system.[22,35,36] Perfectly matched layer absorbing boundary conditions were imposed at the top and bottom of the device structure. Together with the Floquet theorem, the periodic boundary conditions were implemented at the transverse sides (front, back, left and right sides) of OSC devices. The optical properties of LPR and SPR together with the hybridization of quasi-guided and plasmonic modes were fully taken into account in this model.

Supporting Information

Supporting Information is available from the Wiley Online Library or from the author.

Acknowledgements

The project is supported in part by grants (nos. 712010 and 10401466) from the Research Grant Council of the Hong Kong Special Administrative Region, China, and the University Grant Council (UGC) of the University of Hong Kong. This project is also partially supported by a Hong Kong UGC Special Equipment Grant (SEG HKU09). J.H.H. and Y.F.L. acknowledge financial support by the National High-tech R&D Program of China (863 Program, no. 2011AA050523), the Chinese Academy of Sciences, and the National Natural Science Foundation of China (NSFC) (nos. 51173189 and 91023039). Y. Yang acknowledge financial support from the US Office of Naval Research (grant #N00014-04-0434).

Received: January 10, 2012
Revised: March 13, 2012
Published online: May 8, 2012

[1] S. H. Park, A. Roy, S. Beaupré, S. Cho, N. Coates, J. S. Moon, D. Moses, M. Leclerc, K. Lee, A. J. Heeger, *Nat. Photonics* **2009**, *3*, 297.
[2] H. Y. Chen, J. H. Hou, S. Q. Zhang, Y. Y. Liang, G. W. Yang, Y. Yang, L. P. Yu, Y. Wu, G. Li, *Nat. Photonics* **2009**, *3*, 649.
[3] D. Wöhrle, D. Meissner, *Adv. Mater.* **1991**, *3*, 129.
[4] P. W. M. Blom, V. D. Mihailetchi, L. J. A. Koster, D. E. Markov, *Adv. Mater.* **2007**, *19*, 1551.
[5] H. A. Atwater, A. Polman, *Nat. Mater.* **2010**, *9*, 205.
[6] K. S. Nalwa, J. M. Park, K. M. Ho, S. Chaudhary, *Adv. Mater.* **2011**, *23*, 112.
[7] L. Huo, S. Zhang, X. Guo, F. Xu, Y. Li, J. Hou, *Angew. Chem. Int. Ed.* **2011**, *50*, 9697.
[8] D. D. S. Fung, L. F. Qiao, W. C. H. Choy, C. D. Wang, W. E. I. Sha, F. X. Xie, S. L. He, *J. Mater. Chem.* **2011**, *21*, 16349.
[9] D. H. Wang, D. Y. Kim, K. W. Choi, J. H. Seo, S. H. Im, J. H. Park, O. O. Park, A. J. Heeger, *Angew. Chem. Int. Ed.* **2011**, *50*, 5519.
[10] W. E. I. Sha, W. C. H. Choy, W. C. Chew, *Opt. Lett.* **2011**, *36*, 478.
[11] C. C. D. Wang, W. C. H. Choy, C. Duan, D. D. S. Fung, W. E. I. Sha, F. X. Xie, F. Huang, Y. Cao, *J. Mater. Chem.* **2012**, *22*, 1206.
[12] F. X. Xie, W. C. H. Choy, C. C. D. Wang, W. E. I. Sha, D. D. S. Fung, *Appl. Phys. Lett.* **2011**, *99*. 153304.
[13] D. H. Wang, K. H. Park, J. H. Seo, J. Seifter, J. H. Jeon, J. K. Kim, J. H. Park, O. O. Park, A. J. Heeger, *Adv. Energy Mater.* **2011**, *1*, 766.
[14] J. Yang, J. B. You, C. C. Chen, W. C. Hsu, H. R. Tan, X. W. Zhang, Z. R. Hong, Y. Yang, *ACS Nano* **2011**, *5*, 6210.
[15] Y. S. Hsiao, F. C. Chien, J. H. Huang, C. P. Chen, C. W. Kuo, C. W. Chu, P. L. Chen, *J. Phys. Chem. C* **2011**, *115*, 11864.
[16] A. P. Kulkarni, K. M. Noone, K. Munechika, S. R. Guyer, D. S. Ginger, *Nano Lett.* **2010**, *10*, 1501.
[17] J. H. Lee, D. W. Kim, H. Jang, J. K. Choi, J. Geng, J. W. Jung, S. C. Yoon, H.-T. Jung, *Small* **2009**, *5*, 2139.
[18] V. E. Ferry, M. A. Verschuuren, H. B. B. T. Li, R. E. I. Schropp, H. A. Atwater, A. Polman, *Appl. Phys. Lett.* **2009**, *95*, 183503.
[19] J. N. Munday, H. A. Atwater, *Nano Lett.* **2011**, *11*, 2195.
[20] W. Wang, S. M. Wu, K. Reinhardt, Y. L. Lu, S. C. Chen, *Nano Lett.* **2010**, *10*, 2012.
[21] A. Baba, K. Wakatsuki, K. Shinbo, K. Kato, F. Kaneko, *J. Mater. Chem.* **2011**, *21*, 16436.
[22] W. E. I. Sha, W. C. H. Choy, W. C. Chew, *Opt. Express* **2010**, *18*, 5993.
[23] S. I. Na, S. S. Kim, J. Jo, S. H. Oh, J. Kim, D. Y. Kim, *Adv. Funct. Mater.* **2008**, *18*, 3956.
[24] L. S. Roman, O. Inganäs, T. Granlund, T. Nyberg, M. Svensson, M. R. Andersson, J. C. Hummelen, *Adv. Mater.* **2000**, *12*, 189.
[25] E. Wang, Z. Ma, Z. Zhang, K. Vandewal, P. Henriksson, O. Inganäs, F. Zhang, M. R. Andersson, *J. Am. Chem. Soc.* **2011**, *133*, 14244.
[26] J. Hou, H. Y. Chen, S. Zhang, R. I. Chen, Y. Yang, Y. Wu, G. Li, *J. Am. Chem. Soc.* **2009**, *131*, 15586.
[27] M. Heo, H. Cho, J. W. Jung, J. R. Jeong, S. Park, J. Y. Kim, *Adv. Mater.* **2011**, *23*, 5689.
[28] C. H. Kim, S. H. Cha, S. C. Kim, M. Song, J. Lee, W. S. Shin, S. J. Moon, J. H. Bahng, N. A. Kotov, S.-H. Jin, *ACS Nano* **2011**, *5*, 3319.
[29] J. A. Schuller, E. S. Barnard, W. S. Cai, Y. C. Jun, J. S. White, M. L. Brongersma, *Nat. Mater.* **2010**, *9*, 193.
[30] I. K. Ding, J. Zhu, W. S. Cai, S. J. Moon, N. Cai, P. Wang, S. M. Zakeeruddin, M. Grätzel, M. L. Brongersma, Y. Cui, M. D. McGehee, *Adv. Energy Mater.* **2011**, *1*, 52.
[31] D. Gupta, S. Mukhopadhyay, K. S. Narayan, *Sol. Energy Mater. Sol. Cells* **2010**, *94*, 1309.
[32] S. R. Cowan, R. A. Street, S. Cho, A. J. Heeger, *Phys. Rev. B* **2011**, *83*, 035205.
[33] V. D. Mihailetchi, J. Wildeman, P. W. M. Blom, *Phys. Rev. Lett.* **2005**, *94*, 126602.
[34] X. Li, G. Chen, L. Yang, Z. Jin, J. Liu, *Adv. Funct. Mater.* **2010**, *20*, 2815.
[35] W. E. I. Sha, W. C. H. Choy, Y. Wu, W. C. Chew, *Opt. Express* **2012**, *20*, 2572.
[36] X. Li, W. E. I. Sha, W. C. H. Choy, D. D. S. FungF. Xie, *J. Phys. Chem. C* **2012**, *116*, 7200.